

## Research Article

# Finite Element Analysis and Lightweight Optimization Design on Main Frame Structure of Large Electrostatic Precipitator

Xuewen Wang , Bo Li , and Zhaojian Yang 

*Shanxi Key Laboratory of Fully Mechanized Coal Mining Equipment, College of Mechanical Engineering, Taiyuan University of Technology, Taiyuan 030024, China*

Correspondence should be addressed to Xuewen Wang; wxuew@163.com

Received 10 October 2017; Revised 2 November 2017; Accepted 6 November 2017; Published 8 January 2018

Academic Editor: Antonio Gilson Barbosa de Lima

Copyright © 2018 Xuewen Wang et al. This is an open access article distributed under the Creative Commons Attribution License, which permits unrestricted use, distribution, and reproduction in any medium, provided the original work is properly cited.

The geometric modeling and finite element modeling of the whole structure of an electrostatic precipitator and its main components consisting of top beam, column, bottom beam, and bracket were finished. The strength calculation was completed. As a result, the design of the whole structure of the electrostatic precipitator and the main components were reasonable, the structure was in a balance state, its working condition was safe and reliable, its stress variation was even, and the stress distribution was regular. The maximum von Mises stress of the whole structure is 20.14 MPa. The safety factor was large, resulting in a waste of material. An optimization mathematical model is established. Using the ANSYS first-order method, the dimension parameters of the main frame structure of the electrostatic precipitator were optimized. After optimization, more reasonable structural design parameters were obtained. The model weight is 72,344.11 kg, the optimal weight is 49,239.35 kg, and the revised weight is 53,645.68 kg. Compared with the model weight, the optimal weight decreased by 23,104.76 kg and the objective function decreased by 31.94%, while the revised weight decreased by 18,698.43 kg and the objective function decreased by 25.84%.

## 1. Introduction

The control of industrial pollution emissions and the treatment of industrial flue gas pollution are the most important measures of environmental protection. With the advantages of high dusting efficiency, convenience management, low fault rate, and strong adaptability, the electrostatic precipitator (ESP) is widely applied for industrial flue gas treatment in nonferrous metals, metallurgy, construction materials, coal, petrochemicals, and electricity [1–6].

The large electrostatic precipitator is usually composed of dust-precipitator shell (main frame structure), inlet and outlet smoke box, ash storage system, anode and cathode system, rapping device and power supply part, stair platform, and insulation shell part.

The main frame structure is usually composed of top box beam and roof slab, column and side wall, bottom beam, and bracket, which are used for bearing and sealing of electrostatic precipitator, also used as the space for installation and positioning of other parts. The top beam,

column, bottom beam, and bracket constitute spatial mechanical rigid frame. The planar frames are sealed, linked, fixed, and installed by longitudinal components such as roof slab, side wall, and bottom beam, forming a closed self-balance system, protection system, and spatial load-carrying system. All kinds of load on the electrostatic precipitator, the insulation, and protection of dedusting system are born by the system. With the advantages of small deformation, easy control, good stability, and seismic performance, the structure can bear large load and effectively protect the other internal systems [7, 8].

The relevant study on an electrostatic precipitator is mainly focused on the dusting principle or filtration characteristics [9, 10], the collection efficiency or dusting method [11–13], the collected dust or the particulate matter [14, 15], the analysis of the operating [16, 17], and the electrode system or recovery system [18–20] but ignored the study of its bearing structure [21, 22]. The main frame structure is often designed and transformed by companies with analogy method and empirical design instead of precise and scientific calculation. What's worse, the main structure is designed

only from the aspect of security, ignoring the accounting and evaluation of the cost and other aspects. As a result, the material is wasted enormously, and the products are short of market competitiveness from the aspects of shape and cost, which seriously affects the economic benefits of companies.

In this study, the finite element strength analysis [23, 24] and lightweight optimization design of the main structure of the large electrostatic precipitator were carried out using advanced design technologies such as finite element method, optimization design, and virtual prototype. The purpose is to obtain more scientific structure and more reasonable design parameters. What's more, the design and manufacturing costs could be reduced to improve the market competitiveness of products.

## 2. Geometric Model of the Main Structure

The schematic sketch of the main structure of a certain type of electrostatic precipitator is shown in Figure 1. The main structure of this type of electrostatic precipitator consisted of three parts: top beam, column, bottom beam, and bracket.

**2.1. Top Beam.** The top beam of a certain type of electrostatic precipitator consisted of a wide girder and two narrow girders. With the box structure, the girder was made up of slabs and few I-beam steel cross brackets. Between the steel slab and the steel slab, the steel slab and the bracket were the welding relations.

The dimensions of the wide girder were 6814 mm in length, 1640 mm in width, and 1500 mm in height. The dimensions of the narrow girder were 6814 mm in length, 1040 mm in width, and 1500 mm in height. Geometric models are shown in Figures 2 and 3.

**2.2. Column and Side Wall.** The column with complex structure bears greater load. Every column was a combined member bar, which was made by linking channel steels and angle steels with steel slabs. The height of the column was 8.370 m (Figure 4).

The wide wall was made by welding from steel slabs with the thickness of 5 mm. The channel steels, angle steels, and crescent costal boards were welded on the steel slab.

The column system was made by linking six columns with side walls, consisting of two wide columns and four narrow columns. The column system (Figure 5) was a large steel structural assembly, made by linking three column supports (Figure 6) together. The dimensions of the whole mode were 10.860 m in length, 6.590 m in width, and 8.370 m in height.

**2.3. Bottom Beam and Bracket.** The bottom beam had a frame structure made up of one front mudsill, one back mudsill, one middle mudsill, and two side mudsills. The length of the bottom beam was 10.865 m, the width was 6.614 m, the height was 1.16 m, and the weight was 6.812 t. The main body of front and back mudsills was made by welding channel steel and steel slab together, with channel

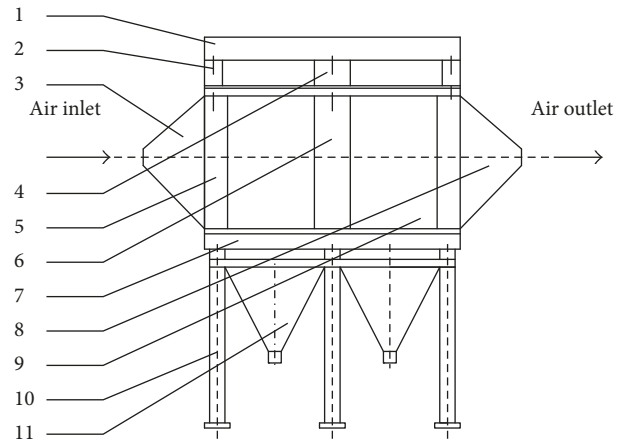


FIGURE 1: The schematic sketch of main structure of electrostatic precipitator. (1) Top lifting cradle, (2) narrow girder, (3) inlet smoke box, (4) wide girder, (5) narrow column, (6) wide column, (7) bottom beam, (8) outlet smoke box, (9) side wall, (10) bottom bracket, (11) ash bucket.

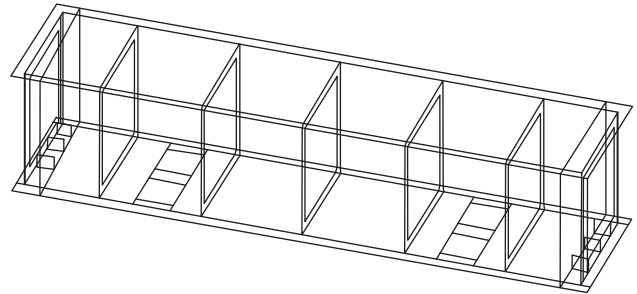


FIGURE 2: The model of the wide girder.

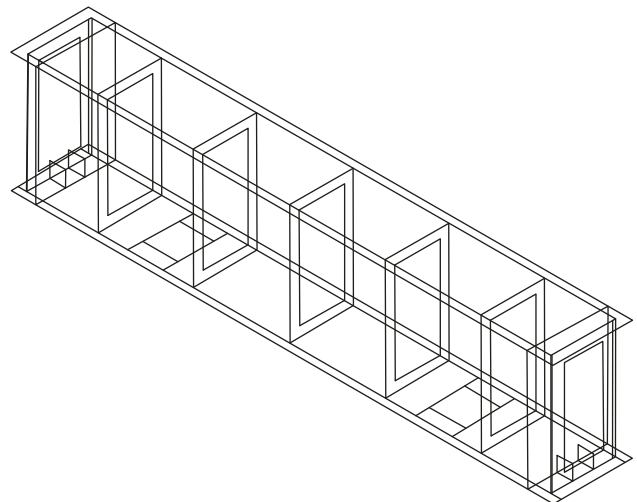


FIGURE 3: The model of the narrow girder.

steel reinforcing plate in the middle and angle steel support frame in upside.

The front and back mudsills were linked with the bottom edge of inlet and outlet smoke box of the electrostatic precipitator. The main body of the side mudsill was also

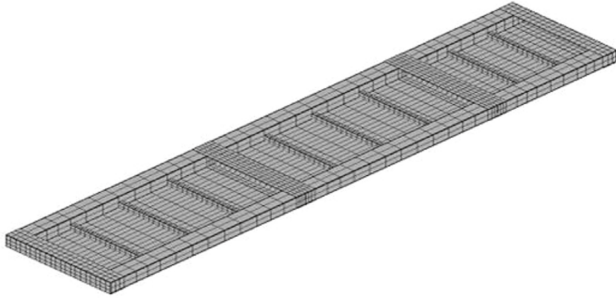


FIGURE 4: The model of the single column.

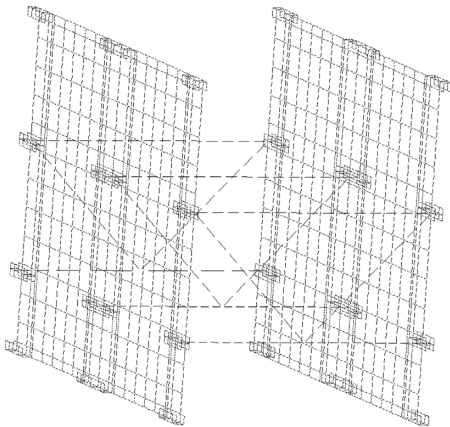


FIGURE 5: The whole model of the column component.

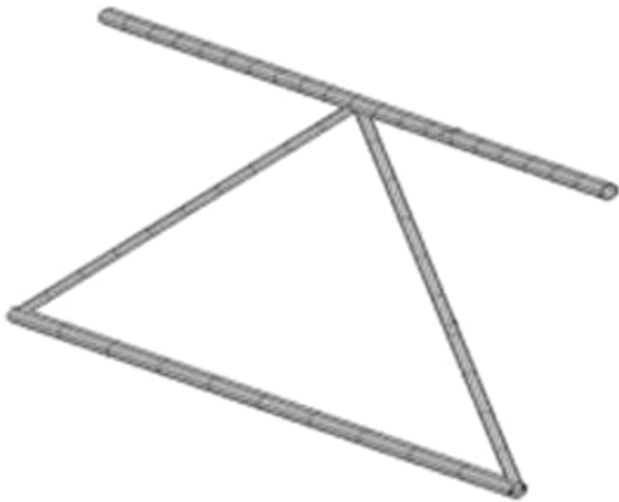


FIGURE 6: The model of column support.

made as a box structure by welding channel steel and steel plate together, in the middle of which was a channel steel reinforcing plate. Taking hot rolled h-shaped steel as prototype design, the middle mudsill was welded in the middle of two side mudsills, forming a framed steel structure with high stiffness and strength (Figure 7).

The mode of the bracket is shown in Figure 8. The bracket was made by linking six pillars as the main body, I

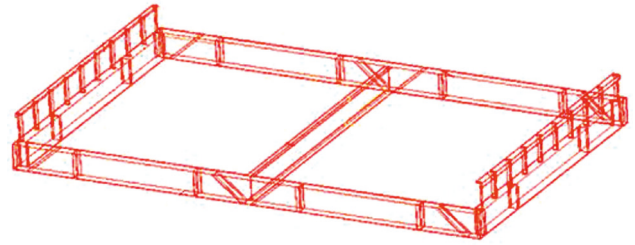


FIGURE 7: The model of the bottom beam.

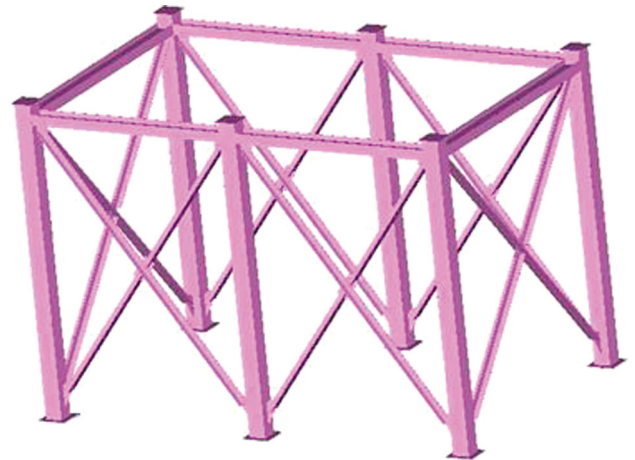


FIGURE 8: The model of the bracket.

steel as cross linking components, and two-L abreast angle steel frame as support. The pillar was made by welding from slabs. The total length of the bracket was 11.050 m, the total width was 7.040 m, the total height was 7.520 m, and the weight was 13.899 t. The bracket with this structure has enough stiffness, strength, and good stability.

The bottom beam was at the top of the bracket. The solid model after assembly is shown in Figure 9.

**2.4. Whole Structure.** The whole solid model of the main structure of a certain type of electrostatic precipitator is shown in Figure 10, and the dimensions were 14 m long, 8.5 m wide, and 22 m high. The space structure of the electrostatic precipitator was reproduced virtually and realistically by a virtual model. The geometry of structural appearance and spatial assembly relation could also be reflected.

### 3. Finite Element Modeling

**3.1. Element Type.** The structure of the large electrostatic precipitator was complex, and its geometric model has block structure, plate structure, cylindrical structure, and tubular structure. Thus, many element couplings were used for building the realistic finite element model of the electrostatic precipitator. The ANSYS built-in elements used in the analysis of this study were as follows.

- (1) Element SHELL63 [25, 26]: the electrostatic precipitator had many slab structures such as cover

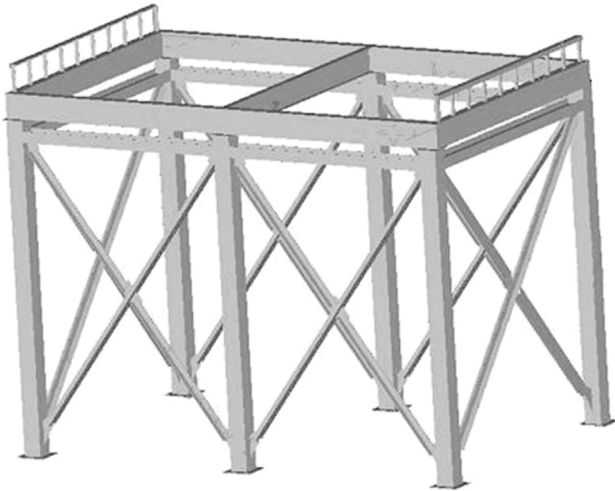


FIGURE 9: The assembly model of the bottom beam and bracket.

plate, web plate, filling-up plate, and diaphragm plate of top beam parts and connecting plate, side wall plate, and storage ash strickle plate outside column. The sizes of those slab structures in length and width direction were much larger than that in thickness direction. For the relative thickness of those slab structures was small, the analysis was mainly aimed at the static strength, while the transverse shear deformation was not very important. The simulation was carried out by using element SHELL63.

- (2) Element BEAM188 [27, 28]: the beam element was used for analyzing the structures standing lateral or transverse load, such as the column of electrostatic precipitator and the main load-carrying components of the supporting column. The ratio of length to cross-sectional area was larger, which was the characteristic of those structures. The BEAM188 element was used for simulating the rod and beam components of the main structure.
- (3) Element SOLID45 [29–31]: some components of the main structure of the electrostatic precipitator were three-dimensional solid block structure, such as bottom beam and support body part. The element SOLID45 was selected for simulating those structures.

**3.2. Finite Element Model.** According to the geometric complexity of different parts of main structure of electrostatic precipitator, structured and unstructured grids were used synthetically in the finite element model [32–35].

In the process of the grid, to effectively balance the calculation accuracy and the calculation scale, the following principles were considered: appropriate number of grids, reasonable mesh density, appropriate element order, high mesh quality, correctly handled grid interface and the boundary point, ensured displacement compatibility, the overall layout of the grid, and reasonable numbered node and unit.

The finite element analysis models of some parts of the main structure of the electrostatic precipitator are shown in Figures 11–13. The finite element analysis of the main structure of the electrostatic precipitator is shown in Figure 14.

#### 4. Finite Element Analysis

The main structure material of the electrostatic precipitator was Q235 steel, and the material properties are shown in Table 1.

**4.1. Top Beam.** The top beam mainly consisted of a wide girder and two narrow girders.

According to the loading characteristics and the actual working conditions of the load-carrying girder of a certain type of electrostatic precipitator, the load acted on the girder could be transformed into 4 types: static load, live load, snow load, and temperature load. The live load consisted of the people load, ash load and so on, which was external load acting on the girders. The snow load was carried by the snow. Because the girders were working in a certain temperature environment, the temperature load needed to be applied in the calculation.

The static load which girders bear mainly consisted of deadweight, roof slab, anode system, cathode system, top crane, grooved plate system, and transformer. Load values of the girder are shown in Table 2.

According to the actual connection between the girders and other structures of the electrostatic precipitator, the translation and rotational freedom in the X and Y direction at one end of girders was restrained, and then the translation and rotational freedom in the Z direction were released. The rotational freedom in the X direction and the translation and the rotational freedom in the Z direction at other end of girders were released.

Results for stress values are shown in Tables 3–5, and the negative represented direction. The stress values of three girders were less than the yield limit of the material, and the girders were in safe working condition.

The von Mises stress nephogram of girders is shown in Figures 15–17. From Figures 15–17, for the upper cover plate was more complex and bearing more load, a greater stress area was concentrated in some parts of the upper cover plate. There were lesser stress values in lower cover plate, web plate, and filling-up plate.

In conclusion, the stress values of the three girders were within failure stress. The stress variation was smooth, and the stress distribution was regular. So the structure design was reasonable. In addition to the upper cover plate, the safety factor of other structures such as web plate, filling-up plate, lower cover plate, inner reinforcing plate, and diaphragm plate was large. The stress values of those structures were much less than the yield limit of the material, which resulted in the material waste. So the lightweight optimization design was feasible.

**4.2. Column.** The column system was made by linking six columns with side walls. The column was the key bearing

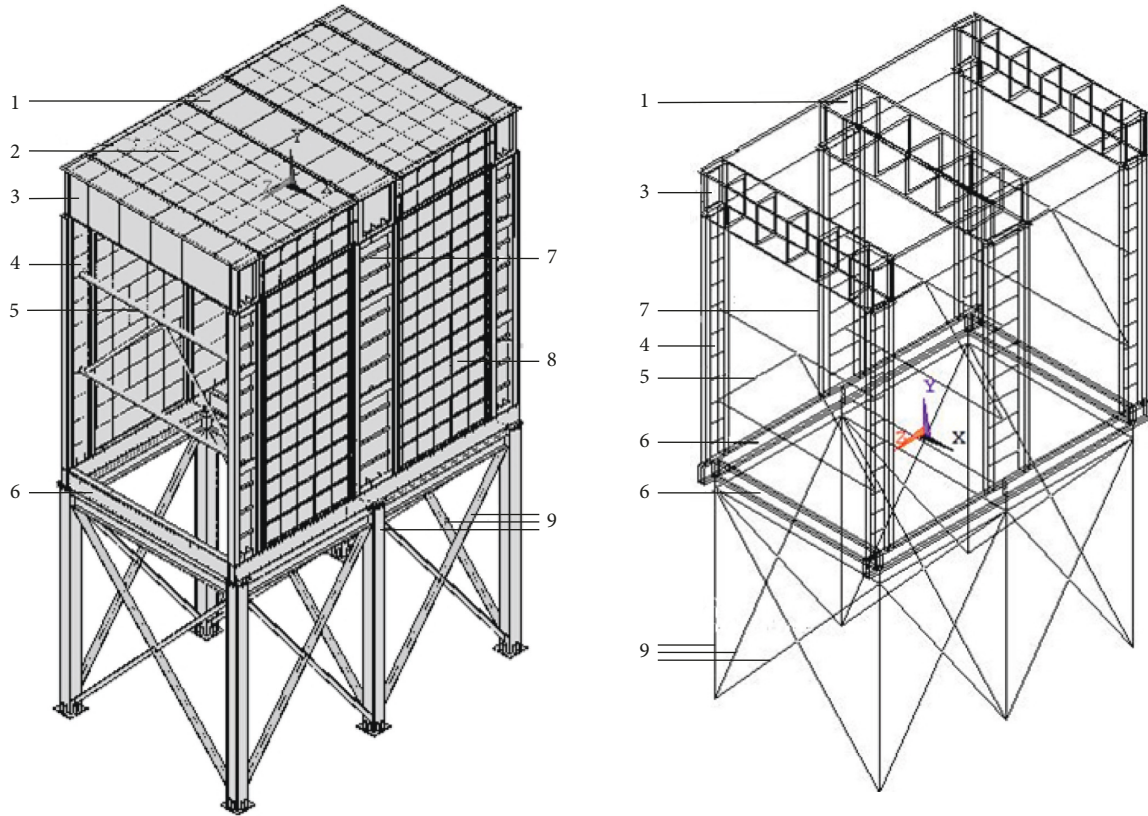


FIGURE 10: The solid model of main structure of the larger electrostatic precipitator. (1) Wide girder, (2) roof slab, (3) narrow girder, (4) narrow column, (5) column support, (6) bottom beam, (7) wide column, (8) side wall slab, (9) bracket.

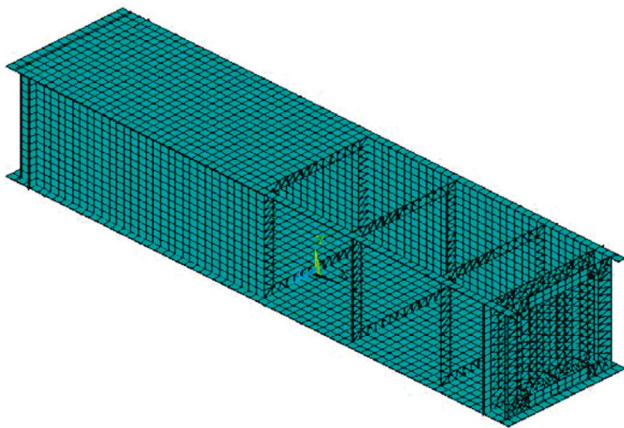


FIGURE 11: The finite element model of girder.

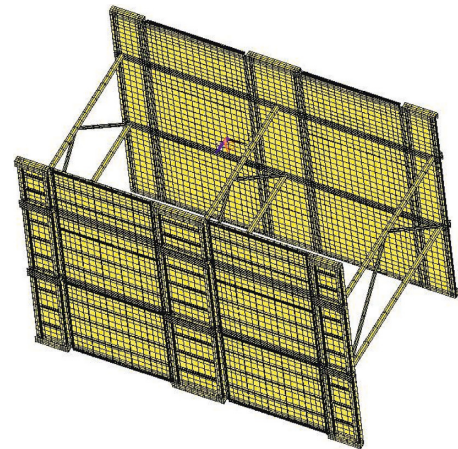


FIGURE 12: The finite element model of column, column support, and side wall.

component of electrostatic precipitator, which bore various loads of electrostatic precipitator, including static load, live load, snow load, and temperature load.

The static load which column system bears mainly consisted of the deadweight and the weight of girder, roof slab, anode system, cathode system, top crane, inlet and outlet smoke box, grooved plate system, and insulation layer. Load values of the column are shown in Table 6.

According to the actual connection between the column system and other structures of the electrostatic precipitator, all DOF of the column and the leftmost node outside the

bottom surface of the side wall was restrained. The translation and rotational freedom in Y and Z direction of the rest nodes outside were restrained, while the translation and rotational freedom in X direction were released. The translation and rotational freedom in X and Z direction of the leftmost node inside were restrained, and the translation and rotational freedom in Z direction of the rest nodes inside were restrained. The translation and rotational freedom in X and Y direction of the column and the leftmost node outside the top surface of side wall were restrained, and the

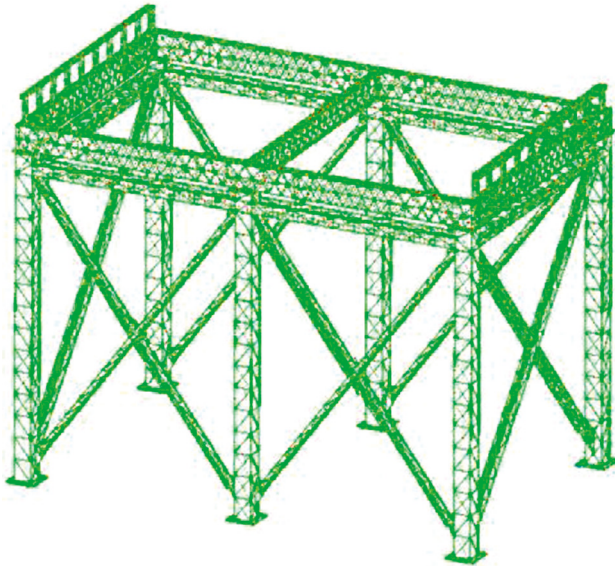


FIGURE 13: The finite element model of the bottom beam and bracket.

translation and rotational freedom in Y direction of the rest nodes inside were restrained.

Results for stress values of column system are shown in Table 7. The maximum stress was less than the failure stress  $\sigma_s$ , and the column system was in safe working condition.

The von Mises stress nephogram of column system is shown in Figure 18. From the figure, the stress value of the total column system was small, and the largest stress value (147 MPa) was in the joint between the column and side wall.

In conclusion, the column system was in the state of balance, and the working condition was safe and reliable. From the von Mises stress nephogram, the stress of the column system changed flatly and was distributed evenly, so the structure design was reasonable. But the safety factor was large, which resulted in the material waste. So the lightweight optimization design was feasible.

**4.3. Bottom Beam and Bracket.** The bottom beam and bracket were under the electrostatic precipitator, as the key bearing components. The bottom beam and bracket bore various loads of electrostatic precipitator, including the deadweight of total electrostatic precipitator, the weight of ash on the polar plates and in the ash bucket, roof live load, negative pressure, wind load, snow load, and temperature load. According to the loading characteristics and the actual working conditions of bottom beam and bracket of electrostatic precipitator, the load which bottom beam and bracket bear could be transformed into 4 types: static load, live load, snow load, and temperature load.

The static load which the bottom beam and bracket bore mainly consisted of their deadweight and the weight of girder, roof slab, anode system, cathode system, top crane, column, side wall, and ash bucket. Load values of the bottom beam and bracket are shown in Table 8.

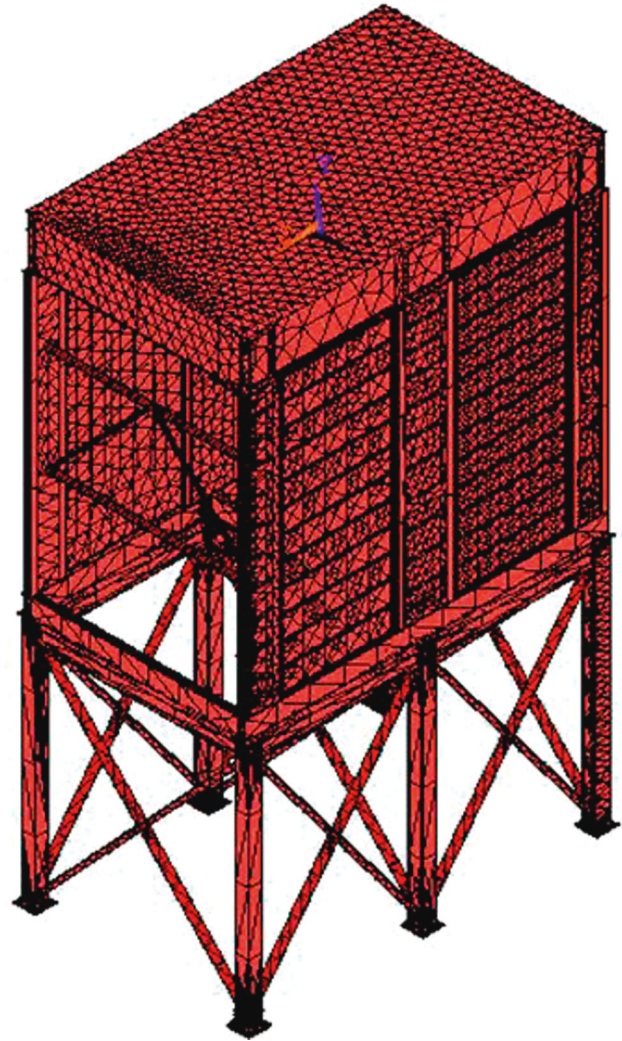


FIGURE 14: The finite element whole model of the overall main structure of the electrostatic precipitator.

TABLE 1: The main structure material properties of the electrostatic precipitator.

| Young modulus           | Material density       | Thermal expansion coefficient | Poisson's ratio | Yield limit |
|-------------------------|------------------------|-------------------------------|-----------------|-------------|
| $2.1 \times 10^{11}$ Pa | 7850 kg/m <sup>3</sup> | $1.22 \times 10^{-5}$         | 0.3             | 185–235 MPa |

TABLE 2: The load information of girders.

|                 | Static load | Snow load | Live load | Temperature load |
|-----------------|-------------|-----------|-----------|------------------|
| Wide girder     | 235638 N    | 2682 N    | 43064 N   | 200°C            |
| Narrow girder 1 | 108482 N    | 1601.25 N | 25620 N   | 200°C            |
| Narrow girder 2 | 150370 N    | 1601.25 N | 25620 N   | 200°C            |

TABLE 3: The maximum principal stress and maximum von Mises stress of the wide girder (Pa).

| $\sigma_1$  | $\sigma_2$  | $\sigma_3$   | von Mises   |
|-------------|-------------|--------------|-------------|
| 0.14329E+09 | 0.10723E+09 | -0.17110E+09 | 0.15219E+09 |

TABLE 4: The maximum principal stress and maximum von Mises stress of the narrow girder in air inlet side (Pa).

| $\sigma_1$    | $\sigma_2$     | $\sigma_3$     | von Mises     |
|---------------|----------------|----------------|---------------|
| $0.37945E+08$ | $-0.27370E+08$ | $-0.53613E+08$ | $0.47672E+08$ |

TABLE 5: The maximum principal stress and maximum von Mises stress of the narrow girder in air outlet side (Pa).

| $\sigma_1$    | $\sigma_2$     | $\sigma_3$     | von Mises     |
|---------------|----------------|----------------|---------------|
| $0.46308E+08$ | $-0.26552E+08$ | $-0.56078E+08$ | $0.49689E+08$ |

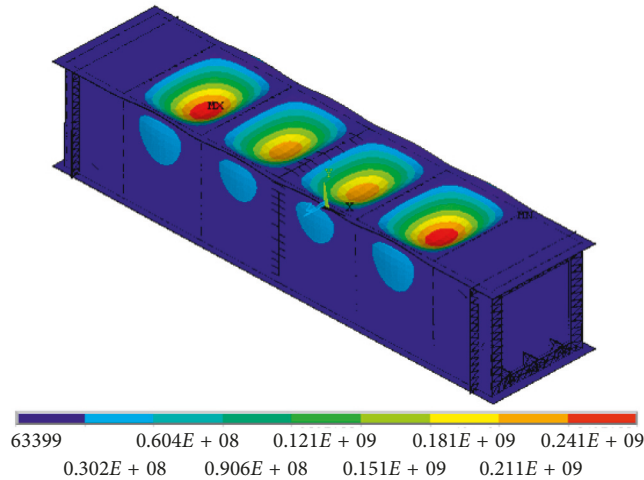


FIGURE 15: The von Mises stress nephogram of the wide girder (Pa).

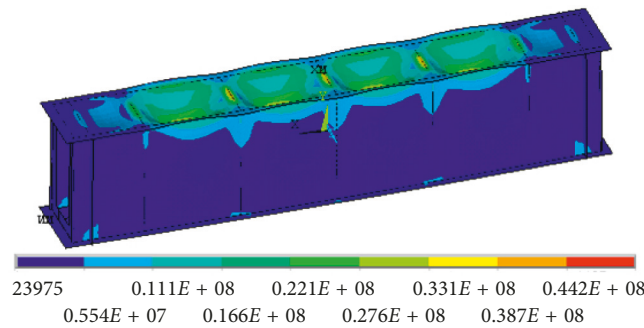


FIGURE 16: The von Mises stress nephogram of the narrow girder in air inlet side (Pa).

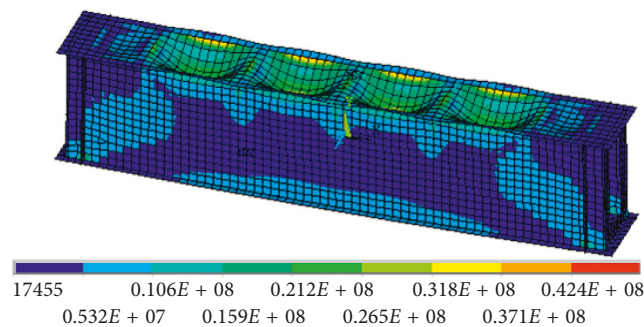


FIGURE 17: The von Mises stress nephogram of the narrow girder in air outlet side (Pa).

TABLE 6: The load information of column.

|                 | Static load | Snow load and live load | Temperature load |
|-----------------|-------------|-------------------------|------------------|
| Wide girder     | 242452 N    | 208250 N                | 200°C            |
| Narrow girder 1 | 192717 N    | 208250 N                | 200°C            |
| Narrow girder 2 | 227820 N    | 208250 N                | 200°C            |

TABLE 7: The maximum principal stress and maximum von Mises stress of column system (Pa).

| $\sigma_1$    | $\sigma_2$     | $\sigma_3$     | von Mises     |
|---------------|----------------|----------------|---------------|
| $0.60356E+08$ | $-0.49690E+08$ | $-0.77296E+08$ | $0.67757E+08$ |

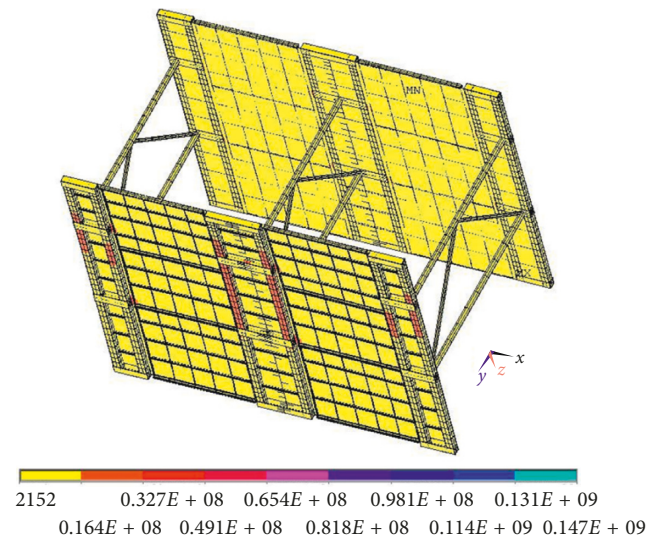


FIGURE 18: The von Mises stress nephogram of the column system (Pa).

According to actual installation requirements of the bottom beam and bracket, the all DOF of the bottom surface of six supports of the bracket was restrained.

Results for stress values of the bottom beam and bracket structure are shown in Table 9. The stress of the bottom beam and bracket was even and mostly less than 10 MPa (Figure 19). The bottom beam and bracket were in the safe working condition, so the structure was reasonable. A large stress area was concentrated inside the joint between the column and bottom beam, which was in accord with the structural characteristics of the bracket.

In conclusion, the stress of the bottom beam and bracket was less than the failure stress. From the stress nephogram, the stress and deformation of the assembly were even and change regularly. The stress and main deformation area were concentrated in the middle mudsill, the front and back mudsill, and the joint between the bracket and bottom beam. So the structure design was reasonable. The structural safety was high and the design was conservative, so the lightweight optimization design was feasible.

4.4. Global Analysis. According to the industry habits, the load of main structure of the electrostatic precipitator was

TABLE 8: The load information of the bottom beam and bracket.

|             |           |           |          |                 |                  |
|-------------|-----------|-----------|----------|-----------------|------------------|
| Static load | Snow load | Live load | Ash load | Ash bucket load | Temperature load |
| 472683 N    | 18466 N   | 295456 N  | 179144 N | 688977 N        | 200°C            |

TABLE 9: The maximum principal stress and maximum von Mises stress of the bottom beam and bracket component (Pa).

|              |              |               |              |
|--------------|--------------|---------------|--------------|
| $\sigma_1$   | $\sigma_2$   | $\sigma_3$    | von Mises    |
| 0.7403E + 05 | 0.2891E + 05 | -0.7324E + 05 | 0.6814E + 05 |

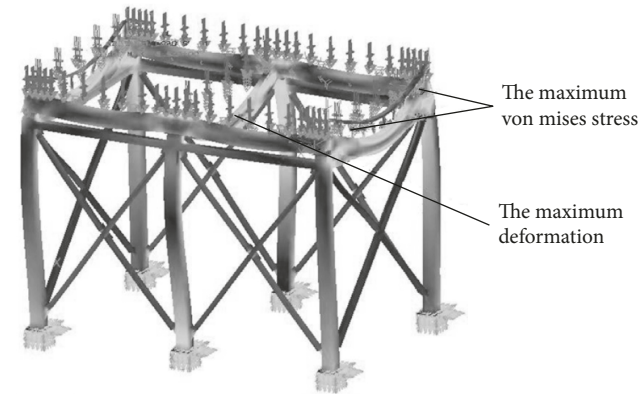


FIGURE 19: The von Mises stress nephogram of the bottom beam and bracket component (Pa).

divided into three types: static load, live load, and temperature load. After assembly of all components, the freedom in the X, Y, and Z direction of the six stand bars of the bracket was restrained. The column components were braced against the mudsills upside bracket, and only the narrow column bottom in the foremost front of the picture was fixed (i.e., the freedom in the X, Y, and Z direction was restrained). The bottom of the other 5 columns was supported by the ball, so that the upper part of the bottom beam can freely stretch in the horizontal direction, reducing additional stress.

From the results in Tables 10–12, the material strength had adequate reserves. The maximum von Mises stress is 20.14 MPa. From the stress nephogram in Figure 20, the stress in the web plate of three girders, roof slab, and side wall slab was small, while the stress in the column, column support, and bracket was larger relatively. Because the structure of the bottom beam was strong, its overall stress was small and changed evenly. The stress in rest parts changed evenly, and the maximum stress was at the joint between the column in the side of positive Z direction and column supports.

In conclusion, the main structure of this type of electrostatic precipitator had adequate reserves. The stress of the total structure was uniform and even, so the structure design was reasonable. However, the safety factor was large, so the lightweight optimization design was feasible.

### 5. Lightweight Optimization Design

5.1. Defining Design Variables. Taking the sizes of the beam, column, bracket plate, and various types of steel sections

TABLE 10: The maximum combined stress (MPa).

|                             |                      |
|-----------------------------|----------------------|
| Stress intensity $\sigma_I$ | von Mises $\sigma_v$ |
| 22.18                       | 20.14                |

TABLE 11: The maximum normal stress and shear stress results (MPa).

|            |            |            |             |             |             |
|------------|------------|------------|-------------|-------------|-------------|
| $\sigma_x$ | $\sigma_y$ | $\sigma_z$ | $\tau_{xy}$ | $\tau_{yz}$ | $\tau_{xz}$ |
| -8.70      | -21.46     | -11.00     | 4.03        | -4.91       | -4.96       |

TABLE 12: The maximum principal stress results (MPa).

|            |            |            |
|------------|------------|------------|
| $\sigma_1$ | $\sigma_2$ | $\sigma_3$ |
| 8.78       | -9.89      | -21.58     |

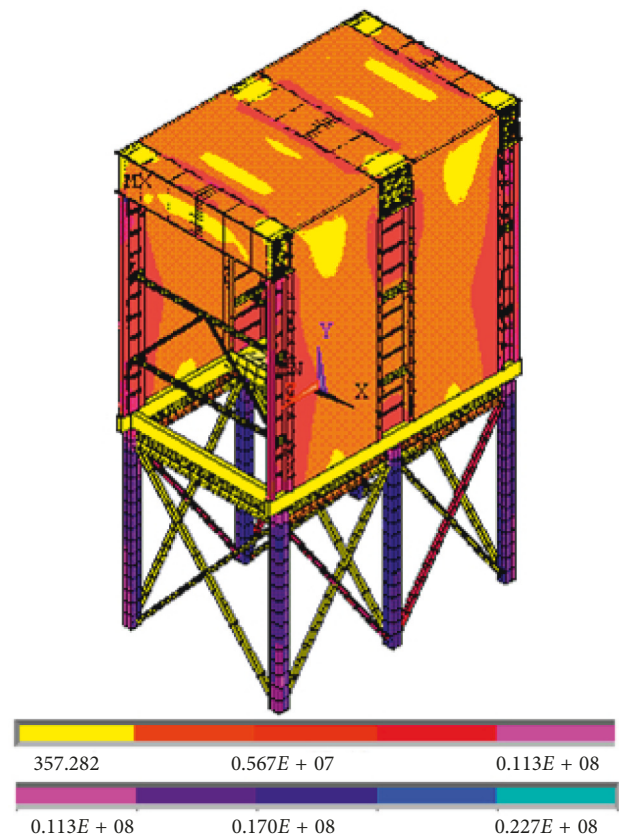


FIGURE 20: The von Mises stress nephogram of the main structure of the electrostatic precipitator (MPa).

as the object, 26 design variables (Table 13) were selected to form the design variable vector  $X = (x_1, x_2, \dots, x_{26})^T$ . Among them, there were 6 variables in the top beam part, 12 in column and side wall part, and 8 in bottom beam and bracket part.

TABLE 13: The optimization results.

| Design variable                          | Optimal value (m) | Revised value (m) | Comments   |   |
|--|-------------------|-------------------|------------|---|
| Top beam<br>(Figures 2 and 3)            | DL_SGB            | $0.300E-2$        | $0.450E-2$ | DL_SGB, DL_XGB, DL_FUB, DL_DUB, DL_GEB1, DL_GEB2, LZ_GB5, LZ_GB12, LZ_H_T, Z_M_T1, Z_M_T2, Z_LZ_T. Due to the limit of width and length, hot rolled heavy steel plate (GB/T709-1998) was selected [36] and those sizes of 0.004 m were all optimized to 0.0045 m;   |
|  | DL_XGB            | $0.300E-2$        | $0.450E-2$ |   |
|  | DL_FUB            | $0.400E-2$        | $0.450E-2$ |   |
|  | DL_DUB            | $0.400E-2$        | $0.450E-2$ |   |
|  | DL_GEB1           | $0.400E-2$        | $0.450E-2$ |   |
|  | DL_GEB2           | $0.400E-2$        | $0.450E-2$ |   |
|  | LZ_GB5            | $0.300E-2$        | $0.450E-2$ |   |
| Column and side wall<br>(Figures 4–6)    | LZ_GB12           | $0.400E-2$        | $0.450E-2$ | LZ_CAO was originally 20# channel steel size. Due to the structural relationship, this channel steel can only choose 20 or 20a channel steel. Therefore, the size of 0.0040045 m was optimized to 20a channel steel size of 0.007 m (GB/T 707-1988) [37]; LZ_H_W was the structure size of the connection between the column and column support. Due to the structural relationship, the size of 0.19 m was optimized to 0.2 m; LZ_J1W, LZ_J1H, LZ_J1D were originally 10/6.3 scalene angle steel 100 × 63 × 6. According to optimization, those sizes were revised to 5/3.2 scalene angle 50 × 32 × 4 (GB/T 9787-1988) [38]; LZ_ZHI_O, LZ_ZHI_I, LZ_LA_O, and LZ_LA_I were the geometric sizes of the column support of contacting column, and the column support was the hollow steel pipe. Taking into account the choice of materials, those sizes were revised to 0.086 m, 0.082 m, 0.053 m, and 0.049 m; Z_T_W, Z_T_H, Z_T_T1, and Z_T_T2 were the sizes of the original structure which was composed of two 14# equal-leg angle steel. According to the optimization, the structure was revised to 9# equal-leg angle steel composite structure (GB/T 9787-1988) [38], those sizes were revised, respectively, to 0.180 m, 0.09 m, 0.006 m, and 0.012 m. |
|  | LZ_CAO            | $0.400E-2$        | $0.700E-2$ |   |
|  | LZ_H_W            | 0.190             | 0.200      |   |
|  | LZ_H_T            | $0.400E-2$        | $0.450E-2$ |   |
|  | LZ_J1W            | $0.310E-1$        | $0.320E-1$ |   |
|  | LZ_J1H            | $0.450E-1$        | $0.500E-1$ |   |
|  | LZ_J1D            | $0.300E-2$        | $0.400E-2$ |   |
|  | LZ_ZHI_O          | $0.830E-1$        | $0.860E-1$ |   |
|  | LZ_ZHI_I          | $0.820E-1$        | $0.820E-1$ |   |
|  | LZ_LA_O           | $0.500E-1$        | $0.530E-1$ |   |
| Bottom beam and bracket<br>(Figures 7–9) | LZ_LA_I           | $0.490E-1$        | $0.490E-1$ |   |
|  | Z_M_T1            | $0.400E-2$        | $0.450E-2$ |   |
|  | Z_M_T2            | $0.400E-2$        | $0.450E-2$ |   |
|  | Z_T_W             | 0.145             | 0.180      |   |
|  | Z_T_H             | $0.850E-1$        | $0.900E-1$ |   |
|  | Z_T_T1            | $0.400E-2$        | $0.600E-2$ |   |
|  | Z_T_T2            | $0.913E-2$        | $0.120E-1$ |   |
|  | Z_LZ_T            | $0.400E-2$        | $0.450E-2$ |   |
|  | Z_LZ_H            | 0.240             | 0.280      |   |
| WT (kg)                                  | 49,239.35         | 53,645.68         |            |   |

Model weight: 72,344.11 kg; optimal weight: 49,239.35 kg (compared with the model weight, the optimal weight decreased by 23,104.76 kg and the objective function decreased by 31.94%); revised weight: 53,645.68 kg (compared with the model weight, the revised weight decreased by 18,698.43 kg and the objective function decreased by 25.84%).

The design variables of DL\_SGB, DL\_XGB, DL\_FUB, DL\_DUB, DL\_GEB1, and DL\_GEB2 belong to the top beam (Figures 2 and 3).

The design variables of LZ\_GB5, LZ\_GB12, LZ\_CAO, LZ\_H\_W, LZ\_H\_T, LZ\_J1W, LZ\_J1H, LZ\_J1D, LZ\_ZHI\_O, LZ\_ZHI\_I, LZ\_LA\_O, and LZ\_LA\_I belong to the column and side wall (Figures 4–6).

The design variables of Z\_M\_T1, Z\_M\_T2, Z\_T\_W, Z\_T\_H, Z\_T\_T1, Z\_T\_T2, Z\_LZ\_T, and Z\_LZ\_H belong to the bottom beam and bracket (Figures 7–9).

**5.2. Defining State Variables.** The state variable was the maximum von Mises stress SMAX. SMAX only defined the upper limit. The material of main structure was Q235 steel, and the yield limit (failure stress) of the material was 185~235 MPa. According to numerous experiment and engineering practice results, the plastic material safety coefficient in static load conditions was 1.2–1.5. Therefore, according to  $(\sigma) = \sigma_s/n_s$ , the material allowable stress ( $\sigma$ ) take a conservative value  $185 \div 1.5 \approx 120$  MPa, that was  $SMAX = (\sigma) = 120$  MPa.

**5.3. Defining Objective Function.** The total weight WT was set as the objective function to be minimized, which was a function of the design variables.

The objective function did not need a given range, but it needed to be given a convergence tolerance. The convergence tolerance of WT was set to 10 kg.

**5.4. Result Analysis.** In the optimization calculation, a total of 25 iteration cycles were designed, forming 25 design sequences. Those sequences were all feasible designs, and the structural weight was optimized in the twenty-third design sequence.

Figure 21 is the objective function curve. From the figure, the weight of the structure decreased steadily and finally tended to the best design, achieving the lightest structure.

Figure 22 is the state variable curve. From the figure, with the decline of the objective function, the state variables increased gradually but did not exceed the allowable stress 120 MPa. It could be seen that all design sequences were of feasible design, and the maximum stress value tended to be stable in the last few iterations and finally achieved the optimal design.

After finishing arranging the result data, from Table 13, it could be seen that the effect of lightweight optimization design was obvious. The total structure weight of the simplified model was 72,344.11 kg. After optimization, compared with the simplified model, the total structure weight

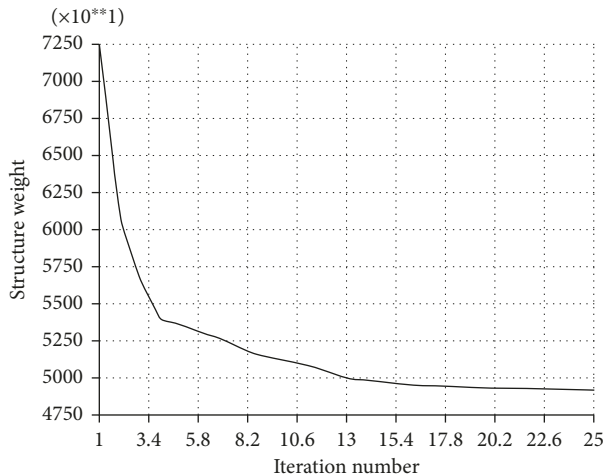


FIGURE 21: The objective function curve.

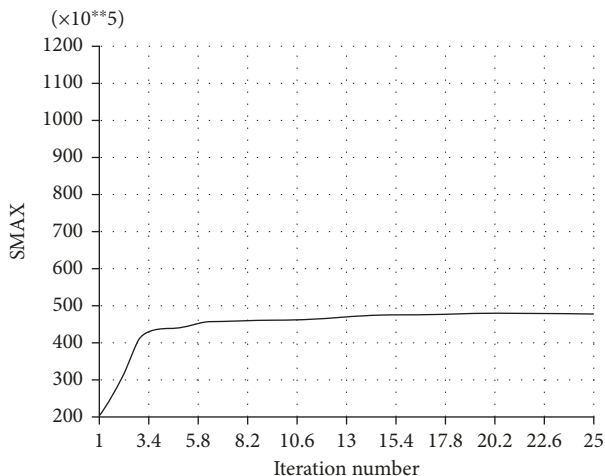


FIGURE 22: The state variable curve.

was reduced by 31.94% and the total weight decreased by about 25.84% after rounding off the parameter values.

## 6. Conclusion

- (1) The geometric modeling and finite element modeling of the whole structure of the electrostatic precipitator and main components consisting of top beam, column, bottom beam, and bracket were finished in this study. Based on detailed discussion of load transfer information and boundary simulation, the strength calculation was completed. As a result, the design of the whole structure of electrostatic precipitator and the main components were reasonable. In the work, the structure was in a balanced state, and the working condition was safe and reliable. The stress was flat. The stress variation was even, and the stress distribution was regular. However, the safety factor was large, resulting in a waste of material, and the lightweight optimization design was feasible.

- (2) On the basis of finite element analysis and CAE optimization analysis method, the dimension parameters of the main whole structure model of electrostatic precipitator were optimized. After optimization, more reasonable structural design parameters were obtained. The model weight is 72,344.11 kg, the optimal weight is 49,239.35 kg, and the revised weight is 53,645.68 kg. Compared with the model weight, the optimal weight decreased by 23,104.76 kg and the objective function decreased by 31.94%, while the revised weight decreased by 18,698.43 kg and the objective function decreased by 25.84%.

## Conflicts of Interest

The authors declare that they have no financial and personal relationships with other people or organizations that can inappropriately influence their work, and there is no professional or other personal interest of any nature or kind in any product, service, and/or company that could be construed as influencing the position presented in the manuscript.

## Acknowledgments

This project was supported by the Merit Funding for the Returned Overseas Personnel Sci-Tech Activities, Shanxi Province, China (Grant no. 2016), Shanxi Scholarship Council of China (2016-043), Program for the Outstanding Innovative Teams of Higher Learning Institutions of Shanxi (2014), and the Basic Condition Platform Project of Shanxi (2014091016).

## References

- [1] J. Huang, H. Wang, Y. Shi et al., "Performance of a pilot-scale wet electrostatic precipitator for the control of sulfuric acid mist," *Environmental Science and Pollution Research*, vol. 23, no. 19, pp. 19219–19228, 2016.
- [2] H. Bin, Z. Lin, Y. Yang, L. Fei, L. Cai, and Y. Linjun, "PM<sub>2.5</sub> and SO<sub>3</sub> collaborative removal in electrostatic precipitator," *Powder Technology*, vol. 318, pp. 484–490, 2017.
- [3] Y.-C. Ahn, S.-D. Kim, S.-H. Lee et al., "Physical, chemical and electrical analysis of dust generated from cement plants for dust removal with an electrostatic precipitator," *Korean Journal of Chemical Engineering*, vol. 21, no. 1, pp. 182–186, 2004.
- [4] A. Berhardt, F. Lezsovits, and B. Groß, "Integrated electrostatic precipitator for small-scaled biomass boilers," *Chemical Engineering & Technology*, vol. 40, no. 2, pp. 278–288, 2017.
- [5] J. I. Levy, L. Biton, P. K. Hopke, K. M. Zhang, and L. Rector, "A cost-benefit analysis of a pellet boiler with electrostatic precipitator versus conventional biomass technology: a case study of an institutional boiler in Syracuse, New York," *Environmental Research*, vol. 156, pp. 312–319, 2017.
- [6] F. Kherbouche, Y. Benmimoun, A. Tilmatine, A. Zouaghi, and N. Zouzou, "Study of a new electrostatic precipitator with asymmetrical wire-to-cylinder configuration for cement particles collection," *Journal of Electrostatics*, vol. 83, pp. 7–15, 2016.
- [7] S. Qiao, X. Han, K. Zhou, and W. Li, "Conceptual configuration and seismic performance of high-rise steel braced

- frame,” *Steel and Composite Structures*, vol. 23, no. 2, pp. 173–186, 2017.
- [8] G. Toutant, Y. B. Minouei, A. Imanpour, S. Koboevic, and R. Tremblay, “Stability of steel columns in steel concentrically braced frames subjected to seismic loading,” in *Proceedings of Structures Congress 2017: Buildings and Special Structures*, pp. 143–154, Denver, CO, USA, April 2017.
- [9] C. Huang, X. Ma, M. Wang, Y. Sun, C. Zhang, and H. Tong, “Property of the PVC dust collecting plate used in wet membrane electrostatic precipitator,” *IEEE Transactions on Plasma Science*, vol. 42, no. 11, pp. 3520–3528, 2014.
- [10] Z. Feng, Z. Long, and T. Yu, “Filtration characteristics of fibrous filter following an electrostatic precipitator,” *Journal of Electrostatics*, vol. 83, pp. 52–62, 2016.
- [11] Z. He, E. T. Mohan Dass, and G. Karthik, “Design of electrostatic precipitator to remove suspended micro particulate matter from gas turbine inlet airflow: part I. Experimental study,” *Journal of Aerosol Science*, vol. 108, pp. 14–28, 2017.
- [12] T.-C. Hsiao, H.-C. Chuang, C.-W. Chen, T.-J. Cheng, and Y. C. C. Chien, “Development and collection efficiency of an electrostatic precipitator for in-vitro toxicity studies of nano- and submicron-sized aerosols,” *Journal of the Taiwan Institute of Chemical Engineers*, vol. 72, pp. 1–9, 2017.
- [13] Z. Qi, J. Li, D. Wu, W. Xie, X. Li, and C. Liu, “Particulate matter emission characteristics and removal efficiencies of a low-low temperature electrostatic precipitator,” *Energy & Fuels*, vol. 31, no. 2, pp. 1741–1746, 2017.
- [14] J. Li, X. Li, C. Zhou et al., “Correlation between polycyclic aromatic hydrocarbon concentration and particulate matter during the removal process of a low-low temperature electrostatic precipitator,” *Energy & Fuels*, vol. 31, no. 7, pp. 7256–7262, 2017.
- [15] C. Lanzerstorfer and D. Steiner, “Characterization of sintering dust collected in the various fields of the electrostatic precipitator,” *Environmental Technology*, vol. 37, no. 12, pp. 1559–1567, 2016.
- [16] C. Lu, C. Yi, R. Yi, and S. Liu, “Analysis of the operating parameters of a vortex electrostatic precipitator,” *Plasma Science & Technology*, vol. 19, no. 2, p. 025504, 2017.
- [17] S. Arif, D. J. Branken, R. C. Everson, H. W. J. P. Neomagus, L. A. le Grange, and A. Arif, “CFD modeling of particle charging and collection in electrostatic precipitators,” *Journal of Electrostatics*, vol. 84, pp. 10–22, 2016.
- [18] S. Zou, Y. Liao, S. Xiong, N. Huang, Y. Geng, and S. Yang, “H<sub>2</sub>S-Modified Fe-Ti spinel: a recyclable magnetic sorbent for recovering gaseous elemental mercury from flue gas as a co-benefit of wet electrostatic precipitators,” *Environmental Science & Technology*, vol. 51, no. 6, pp. 3426–3434, 2017.
- [19] T. H. Jun, M. J. Kim, S. Kim, Y. H. Jung, H.-R. Moon, and K.-S. Kim, “Evaluation of activated carbon-coated electrode in electrostatic precipitator and its regeneration for volatile organic compounds removal,” *Water Air and Soil Pollution*, vol. 228, no. 3, p. 110, 2017.
- [20] M. Ali, K. Alam, Y. T. A. Al-Majali, and M. Kennedy, “Novel hybrid composite discharge electrode for electrostatic precipitator,” *Journal of the Air & Waste Management Association*, vol. 67, no. 9, pp. 1036–1045, 2017.
- [21] J. Ji and X. Ding, “Stiffener layout optimization of inlet structure for electrostatic precipitator by improved adaptive growth method,” *Advances in Mechanical Engineering*, vol. 6, p. 979604, 2014.
- [22] R. S. Adhav, A. Samad, and F. Kenyery, “Optimal designs of an ESP to handle upto 10% GVF,” *International Journal of Oil Gas and Coal Technology*, vol. 13, no. 4, pp. 338–358, 2016.
- [23] H. Shinde, A. Sangle, S. Shendkar et al., “Optimization of vibration of collecting plates of electrostatic precipitator through FEA,” in *Lecture Notes in Mechanical Engineering*, pp. 455–460, Springer, Berlin, Germany, 2016.
- [24] N. Hamou, A. Massinissa, A. Hakim, and Z. Youcef, “Finite element method investigation of electrostatic precipitator performance,” *International Journal of Numerical Modelling: Electronic Networks, Devices and Fields*, vol. 28, no. 2, pp. 138–154, 2015.
- [25] M. Aydin Komur and M. Sonmez, “Elastic buckling of perforated plates subjected to linearly varying in-plane loading,” *Structural Engineering and Mechanics*, vol. 28, no. 3, pp. 353–356, 2008.
- [26] D. Coutu, V. Brailovski, and P. Terriault, “Promising benefits of an active-extradors morphing laminar wing,” *Journal of Aircraft*, vol. 46, no. 2, pp. 730–731, 2009.
- [27] Z. Xiao-Shun, Z. Ding-Guo, and C. Si-Jia, “Several dynamic models of a large deformation flexible beam based on the absolute nodal coordinate formulation,” *Acta Physica Sinica*, vol. 65, no. 9, p. 094501, 2016.
- [28] Y.-L. Guo, P. Zhou, M.-Z. Wang, Y.-L. Pi, M. A. Bradford, and J.-Z. Tong, “Experimental and numerical studies of hysteretic response of triple-truss-confined buckling-restrained braces,” *Engineering Structures*, vol. 148, pp. 157–174, 2017.
- [29] G. Vasudevan and S. Kothandaraman, “RC beams retrofitted using external bars with additional anchorages-a finite element study,” *Computers and Concrete*, vol. 16, no. 3, pp. 415–428, 2015.
- [30] G. Vasudevan and S. Kothandaraman, “Finite element analysis of bearing capacity of RC beams retrofitted with external bars,” *Strength of Materials*, vol. 46, no. 6, pp. 831–842, 2014.
- [31] P. Yang, J. Gong, H. Yang, and X. Tang, “Fatigue analysis on thermal characteristics for PBGA by using finite element method,” *Journal of Thermal Stresses*, vol. 37, no. 9, pp. 1052–1065, 2014.
- [32] H. Chen, Z. Lu, and T. Guo, “A hybrid dynamic mesh generation method for multi-block structured grid,” *Advances in Applied Mathematics and Mechanics*, vol. 9, no. 4, pp. 887–903, 2017.
- [33] D. Jarema, H. J. Bungartz, T. Goerler, F. Jenko, T. Neckel, and D. Told, “Block-structured grids in full velocity space for Eulerian gyrokinetic simulations,” *Computer Physics Communications*, vol. 215, pp. 49–62, 2017.
- [34] S. Krishnan, E. S. G. Shaqfeh, and G. Iaccarino, “Fully resolved viscoelastic particulate simulations using unstructured grids,” *Journal of Computational Physics*, vol. 338, pp. 313–338, 2017.
- [35] G. Hu, “A numerical study of 2D detonation waves with adaptive finite volume methods on unstructured grids,” *Journal of Computational Physics*, vol. 331, pp. 297–311, 2017.
- [36] Chinese National Standard-GB/T 709-1988, *Dimension, Shape, Weight and Tolerances for Hot-Rolled Plates and Sheets*, 1988.
- [37] Chinese National Standard-GB/T 707-1988, *Dimension, Shape, Weight and Tolerances for Hot-Rolled Channel Angle Steel*, 1988.
- [38] Chinese National Standard-GB/T 9787-1988, *Dimension, Shape, Weight and Tolerances for Hot-Rolled Equal-Leg Angle Steel*, 1988.



**Hindawi**  
Submit your manuscripts at  
[www.hindawi.com](http://www.hindawi.com)

